Chemical Science

ROYAL SOCIETY OF CHEMISTRY

EDGE ARTICLE

View Article Online
View Journal | View Issue

Cite this: *Chem. Sci.*, 2026, **17**, 5604

All publication charges for this article have been paid for by the Royal Society of Chemistry

A highly effective self-supplying photosensitizer drug for the treatment of deep-tissue metastatic tumors

Hao Zhang,†[a] Hanxiang Li,†[a] Mingchao Xia,[a] Yuhang Wang,[a] Jingyu Zhou,[a] Yue Tang,*[b] Hongyu Wang,*[c] Zhengze Yu*[a] and Bo Tang*[d]

Received 19th November 2025
Accepted 25th December 2025

DOI: 10.1039/d5sc09043a

rsc.li/chemical-science

Due to the inherent defects of photodynamic therapy (PDT), its application in the treatment of deep-tissue metastatic tumors remains challenging. To extend the applicability of PDT, a novel chemiexcited photosensitizer, Cy7-EOM, was developed by covalently coupling the photosensitizer Cy7 with a peroxycatechol derivative and encapsulating it within folate-modified and disulfide-containing nano-micelles. Upon targeted delivery and selective release, positively charged Cy7-EOM would target the mitochondria and efficiently generate singlet oxygen ($^1O_2$) through intramolecular chemical energy transfer (ICET), directly inducing mitochondrial damage and cell apoptosis, realizing an efficient PDT for deep-tissue metastatic tumors. Remarkably, the covalent tethering of the photosensitizer to the peroxyoxalate ensures their spatial proximity to within 1 nm. This configuration profoundly boosts the efficiency of ICET, achieving potent PDT even at low endogenous levels of H_2O_2. Moreover, the tumor-specific decomposition of the nano-micelles eliminates the quenching effect caused by aggregation and removes the diffusion barrier to $^1O_2$, while in normal tissues the integrity of the nano-micelles shields the tissues against the lethal effects of $^1O_2$. This method provides a new strategy for transforming adjuvant photosensitizers into direct therapeutic drugs, with significant potential for clinical application in the treatment of metastatic tumors.

Introduction

In cancer-related mortality, 90% is attributable to cancer metastasis and its associated complications.[1–4] The expected five-year survival rate for patients with metastatic tumors is significantly lower than that of patients with a primary tumor.[5,6] Currently, the clinical treatment of metastatic tumors relies primarily on surgical removal followed by systemic chemotherapy, which are often associated with severe side effects and limited therapeutic efficacy.[7,8] Consequently, effective treatment for deep-seated metastatic tumors remains a major challenge, highlighting the urgent need for the development of novel and more efficient therapeutic strategies and drugs for metastatic tumors. PDT consists of three essential components: photosensitizers, excitation light, and oxygen. This process activates photosensitizers through excitation light of specific wavelength, leading to energy transfer that produces reactive oxygen species (ROS).[9–11] Due to its non-invasive nature, high spatiotemporal selectivity, low systemic toxicity, and favorable therapeutic efficacy, PDT has been applied in clinical cancer treatments.[12,13] However, the limited tissue penetration by the excitation light required by traditional photosensitizers restricts PDT to superficial lesions or those accessible by endoscopy, such as oral, skin, esophageal, gastric, and bladder cancers.[14–18] It is not yet feasible to apply PDT to metastatic tumors in deep tissues. Therefore, the development of novel strategies for *in situ* excited PDT in deep tissues, as well as the expansion of its clinical applications, is of critical importance and urgency.

Since no external light source is needed, chemical energy can be produced *in situ* within tumor tissue and has been used to construct chemiexcited PDT systems.[19–25] Among commonly used substances, peroxycatechol derivatives are particularly favored for chemiexcited PDT.[26] However, a critical challenge in this field is its low efficiency, which results primarily from the nanoscale self-assembly strategies used to construct probes. As we all know, the efficiency of energy transfer is critically dependent on the proximity between the donor and the acceptor.[27] In current research, photosensitizers and bis{3,4,6-trichloro-2-[(pentyloxy)carbonyl]phenyl} oxalate (CPPO) are typically assembled through non-covalent interactions to form

[a]*College of Chemistry and Chemical Engineering, Qingdao University, Qingdao 266071, P. R. China. E-mail: qduyuzz@qdu.edu.cn*

[b]*Department of Emergency Medicine, Shandong Provincial Clinical Research Center for Emergency and Critical Care Medicine, Qilu Hospital of Shandong University, Jinan, 250014, P. R. China. E-mail: yuetang0531@hotmail.com*

[c]*Key Laboratory of Marine Drugs, Ministry of Education, Molecular Synthesis Center, And School of Medicine and Pharmacy, Ocean University of China, Qingdao, 266003, P. R. China. E-mail: why@ouc.edu.cn*

[d]*Lao Shan Laboratory, Qingdao, 266237, P. R. China. E-mail: btang@qnlm.ac*

† These authors contributed equally.

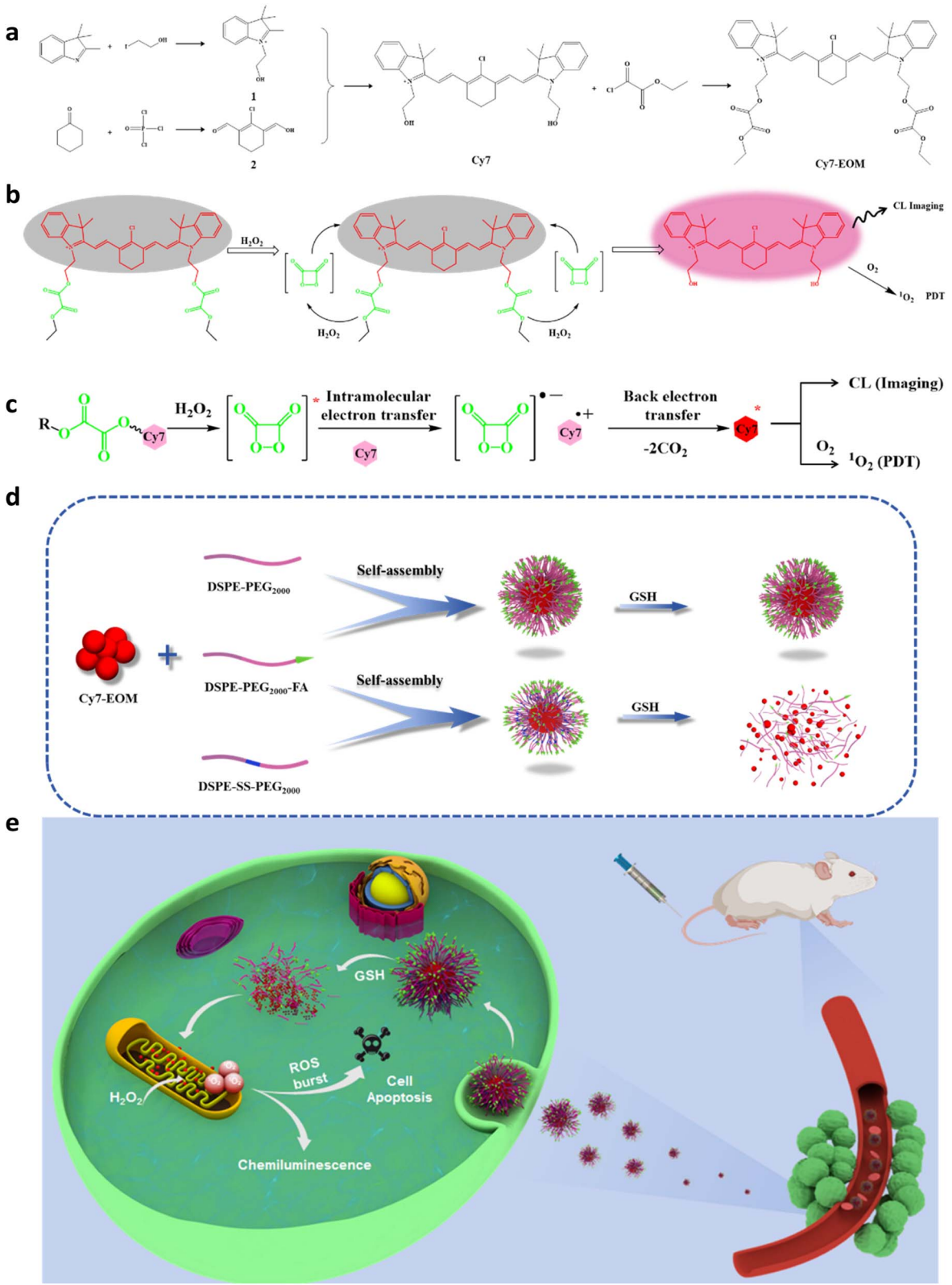

Fig. 1 (a) Synthesis route of Cy7-EOM. Schematic illustration of CL imaging and PDT based on ICET (b), and the detailed mechanism of the CIEEL process (c). Preparation of Cy7-EOM NMs and Cy7-EOM SS NMs and GSH-triggered degradation of Cy7-EOM SS NMs (d), and details of the ICET-based mitochondria targeted PDT against cancer metastasis (e).

nanoscale probes, which then undergo PDT through intermolecular energy transfer.[28–32] However, this probe construction strategy results in an uncontrollable and long distance between the energy donor and acceptor, leading to low energy transfer efficiency.[33–36] Recently, several unimolecular designs have been reported to improve ROS generation based on luminol chemiluminescence.[37–39] However, these approaches failed to address the aggregation caused quenching (ACQ) effect of photosensitizers within the nanomaterials, which seriously reduces ROS production efficiency.[40–42] Even more critically, due to the short lifetime of ROS and short diffusion distance, the nanoscale assembly strategy significantly shields and impedes the diffusion of ROS, leading to a significant loss of ROS.[43,44]

To address the aforementioned challenges, a covalent conjugate of Cy7 and peroxyoxalate was developed as a novel photosensitizer drug (Cy7-EOM) through an esterification reaction of the FDA-approved near-infrared photosensitizer Cy7 and the organic compound ethyl chlorooxoacetate (EOM). Then Cy7-EOM was encapsulated into folate-modified nano-micelles featuring disulfide bonds *via* self-assembly (Cy7-EOM SS NMs). Upon targeting metastatic tumors, Cy7-EOM SS NMs will consume the high intracellular levels of reductive glutathione (GSH) and degrade, releasing the photosensitizer Cy7-EOM, which would specifically target mitochondria due to its positive charge. Under conditions of high endogenous intracellular H_2O_2, Cy7-EOM can be activated *in situ via* an ICET mechanism. It is noteworthy that, compared to intermolecular energy transfer, the covalent coupling of the energy donor with the acceptor significantly reduces the distance to within 1 nm, enabling more efficient energy transfer and ROS generation. The generated ROS will directly induce mitochondrial dysfunction and subsequent apoptosis of cancer cells. Furthermore, the specific decomposition of the nano-micelles in tumor tissue not only prevents the occurrence of the ACQ phenomenon, but eliminates shielding interference with ROS diffusion. Combined with GSH depletion, the efficacy of PDT for deep-tissue metastatic tumors has been synergistically enhanced. In normal tissue, the low redox levels cannot activate the photosensitizer and the nano-micelles can remain intact, which can effectively shield the diffusion of ROS and protect normal tissue from oxidative damage. Thus, an efficient and tumor-selective PDT was achieved for the treatment of metastatic tumors. Compared with luminol chemiluminescence, peroxyoxalate chemiluminescence possesses the advantages of high sensitivity, high quantum efficiency and long luminescence lifetime.[26] As far as we know, this is the first peroxyoxalate-based small-molecule photosensitizer with high efficiency, which can effectively generate ROS under endogenous H_2O_2 without external stimulants or additional H_2O_2. The structure of Cy7-EOM and the Cy7-EOM SS NMs and the details of ICET-based mitochondria targeted PDT against cancer metastasis are illustrated in Fig. 1.

Results and discussion

Design, synthesis and characterization of the photosensitizer

We first designed and synthesized the ICET-based photosensitizer Cy7-EOM, which consists of two components: (1) a peroxyoxalate group, which acts as the chemiluminescence substrate, which can generate a high-energy intermediate, (*i.e.* 1,2-dioxetanedione) by interacting with H_2O_2, and 2) a Cy7 derivative, which serves as a photosensitizer to capture chemical energy upon the deactivation of the unstable intermediate for generation of $^1O_2$. The final product Cy7-EOM was obtained by covalent coupling of EOM and hydroxylated Cy7 through an esterification reaction. The synthetic route of Cy7-EOM and mechanism of ICET-based PDT are illustrated in Fig. 1a and b. The designed Cy7 and Cy7-EOM were successfully characterized by nuclear magnetic resonance (NMR) and high resolution mass spectrometry (HR-MS), respectively (Fig. S1–S6). Thus, the designed photosensitizer could be activated specifically in tumor tissue due to the high levels of intracellular H_2O_2, through a chemically initiated electron exchange luminescence (CIEEL) process (Fig. 1c).[37,45] Whether the photosensitizer Cy7 could be excited by a 1,2-dioxetanedione intermediate was first verified through theoretical calculation. The calculated results showed that the HOMO of Cy7 (−3.50 eV) matched well with the LUMO of 1,2-dioxetanedione (−3.20 eV), indicating its theoretical feasibility (Fig. S7). The response mechanism of Cy7-EOM to H_2O_2 was further clarified using HR-MS (Fig. S8). The chemical connection facilitates the proximity between the donor peroxyoxalate and the acceptor Cy7, resulting in efficient ICET and self-supplying $^1O_2$ without the requirement for an external light source. To achieve targeted delivery and selective release into cancer cells, Cy7-EOM was co-assembled with a folate-modified and disulfide-containing amphiphilic diblock copolymer (DSPE-SS-PEG$_{2000}$: DSPE-PEG$_{2000}$-FA = 2 : 1), yielding aqueous nano-micelles (Cy7-EOM SS NMs). As the control group, nano-micelles without disulfide bonds (Cy7-EOM NMs) were prepared *via* the same methods (DSPE-PEG$_{2000}$: DSPE-PEG$_{2000}$-FA = 2 : 1) (Fig. 1d). Previous research showed that Cy7 containing Cl atoms can attach themselves to serum albumin, resulting in a change in photochemical properties and even fluorescence quenching. Therefore, in this design, nano-micelles also serve as a protective barrier during circulation before the targeted release of Cy7-EOM in cancer cells.[46,47] As shown in the TEM images, both Cy7-EOM SS NMs and Cy7-EOM NMs displayed a spherical morphology with excellent monodispersity (Fig. 2a and S9a). Cy7-EOM SS NMs and Cy7-EOM NMs had similar hydrodynamic diameters according to dynamic light scattering analysis (DLS) and they had neutral surface charge according to zeta potential measurement (Fig. S10 and S11). Due to the specific response of disulfide bonds to GSH, nano-micelles containing disulfide bonds will decompose and release their cargo. TEM images displayed an obvious morphological change in Cy7-EOM SS NMs after incubation with GSH for 3 h, while the morphology of Cy7-EOM NMs remained intact (Fig. 2b and S9b).

Then, the optical properties of Cy7-EOM and relevant nano-micelles were recorded and analyzed. As shown in the absorption spectra, the maximum absorption peak of Cy7-EOM was approximately 774 nm, the same as the Cy7 parent, while that of Cy7-EOM SS NMs was redshifted to 786 nm (Fig. S12). Similarly, fluorescence and chemiluminescence spectra demonstrated that the maximum emission peak of Cy7-EOM was at 803 nm,

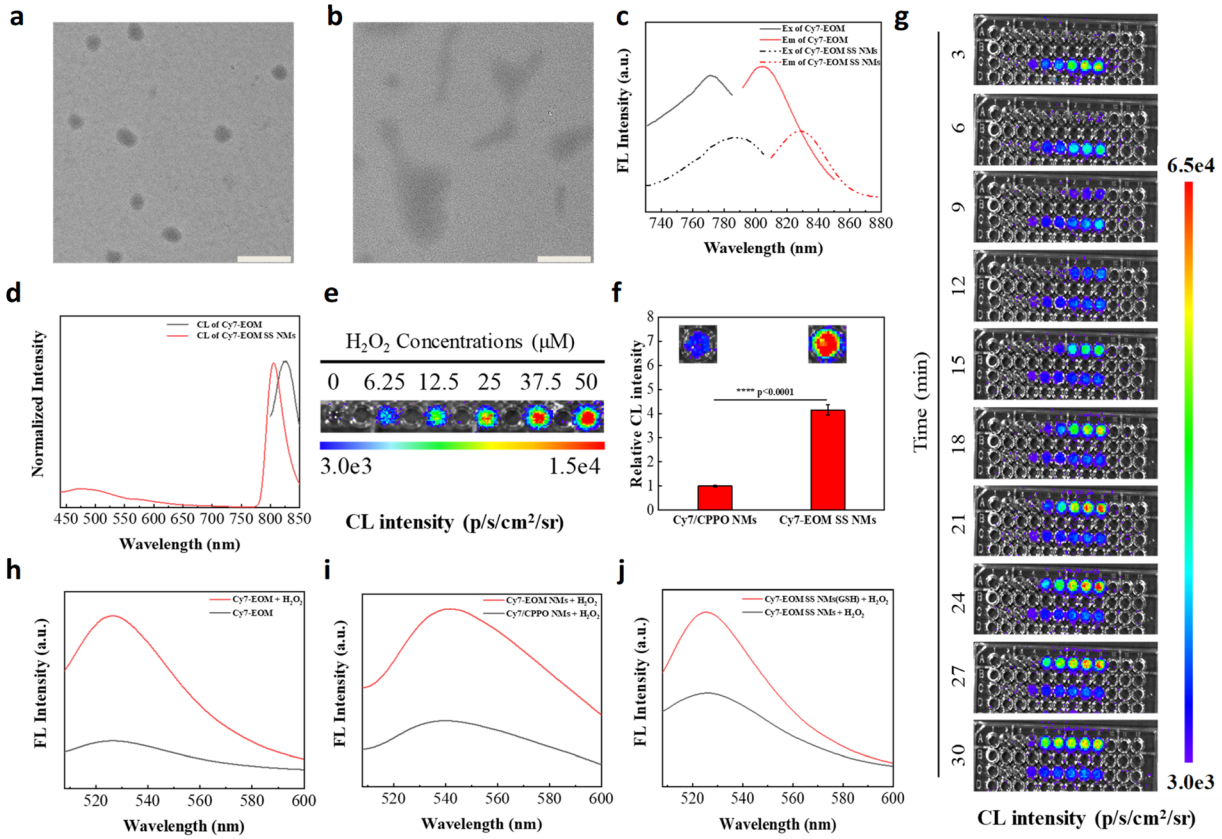

Fig. 2 Characterization of Cy 7-EOM and Cy7-EOM SS NMs. (a) TEM images of Cy7-EOM SS NMs. (b) TEM images of Cy 7-EOM SS NM after incubation with GSH (10 mM) for 3 h. Scale bars are 400 nm. (c) The fluorescence excitation and emission spectra of Cy7-EOM and Cy7-EOM SS NMs. (d) Normalized CL spectra of Cy7-EOM and Cy7-EOM SS NMs. (e) Chemiluminescent image and profile of Cy7-EOM (25 μM) treated with different amounts of H_2O_2 (0, 6.25, 12.5, 25, 37.5, and 50 μM). (f) Relative CL intensity of Cy7/CPPO NMs and Cy7-EOM SS NMs at the same concentration after the addition of H_2O_2 (10 mM), respectively. Insets: corresponding CL images. (g) Time-dependent intensity changes in CL signals of Cy7-EOM SS NMs (upper line in each picture) and Cy7-EOM (bottom line in each picture) with different concentrations of H_2O_2 (from left to right: 0.1, 1.0, 5.0, 10, 25 and 50 mM). The fluorescence spectra of the SOSG probe for the detection of $^1O_2$ production. (h) Cy7-EOM and Cy7-EOM + H_2O_2. (i) Cy7/CPPO NMs + H_2O_2 and Cy7-EOM NMs + H_2O_2. (j) Cy7-EOM SS NMs + H_2O_2 and GSH-pre-treated Cy7-EOM SS NMs + H_2O_2. Data are reported as the means ± S.D. and analyzed by two-tailed Student's *t*-test.

while it was redshifted by about 25 nm after forming nano-micelles (Fig. 2c and d). The FL emission intensity of Cy7-EOM SS NMs was approximately half that of Cy7-EOM at the same concentration, which resulted from aggregation caused quenching (ACQ). Another control group was set up by preparing nano-micelles without disulfide bonds, but loaded with individual Cy7 + CPPO (Cy7/CPPO NMs). Next, the chemiluminescence of Cy7-EOM with different concentrations of H_2O_2 was investigated. Chemiluminescence images indicated that Cy7-EOM has a very good response to a low concentration of H_2O_2, and good linearity between the chemiluminescence signals and H_2O_2 amounts ranging from 0 to 50 μM was observed (Fig. 2e and S13). Moreover, the chemiluminescence intensity of Cy7-EOM SS NMs is much higher than that of Cy7/CPPO NMs, revealing more efficient ICET than intermolecular energy transfer (Fig. 2f). Then, a chemiluminescence dynamic experiment with Cy7-EOM and Cy7-EOM SS NMs with different concentrations of H_2O_2 was also carried out. From the chemiluminescence images, we found that Cy7-EOM has a rapid and concentration-dependent response to H_2O_2, suggesting that effective ICET could be achieved in the designed photosensitizer drug, while the response of Cy7-EOM SS NMs to H_2O_2 showed a lag in time (Fig. 2g). This is mainly due to the shielding effect of the nano-micelle, which hinders effective contact between Cy7-EOM and H_2O_2. Therefore, in the same way, nano-micelles will also hinder the diffusion of low-lifetime ROS produced inside the nanoparticles, leading to the loss of ROS and inefficient PDT. To validate our hypothesis, $^1O_2$ generation in each group was detected using Singlet Oxygen Sensor Green (SOSG). As shown in the fluorescence spectra, the fluorescence intensity of SOSG significantly increased and showed a 5-fold enhancement after H_2O_2 was added to the solution of Cy7-EOM, indicating the generation of $^1O_2$ (Fig. 2h). Moreover, as expected, fluorescent enhancements of SOSG were also observed for Cy7-EOM NMs compared to Cy7/CPPO NMs, demonstrating the superior efficiency of $^1O_2$ generation through ICET to intermolecular energy transfer (Fig. 2i). In addition, GSH-pre-treated Cy7-EOM SS NMs exhibited more $^1O_2$ generation than Cy7-EOM SS NMs without GSH treatment, further confirming that ACQ and the structure of the nano-

micelles could affect the effective utilization of $^1O_2$ (Fig. 2j). Furthermore, electron spin resonance (ESR) spectroscopy was also employed for $^1O_2$ analysis by using a radical scavenger, 2,2,6,6-tetramethylpiperidine (TEMP). The appearance of the characteristic peaks in the ESR spectra after the addition of H_2O_2 demonstrated $^1O_2$ generation and the increased intensity of the ESR signal in the sample of Cy7-EOM further proves that the release of Cy7-EOM from nano-micelles is beneficial to PDT (Fig. S14).

Evaluation of intracellular $^1O_2$ generation

First, chemiluminescence triggered by endogenous H_2O_2 was measured in 4T1 cells without any external stimulants or additional H_2O_2. As shown in the CL images, obvious chemiluminescence was observed in 4T1 cells treated with Cy7-EOM SS NMs and Cy7-EOM NMs, and the CL intensity was positively correlated with cell counts (Fig. 3a and b). Furthermore, the higher CL intensity observed in 4T1 cells treated with Cy7-EOM SS NMs, compared to those treated with Cy7-EOM NMs, indicates that the ACQ effect quenched CL within the nano-micelles, with the subsequent release of Cy7-EOM upon decomposition, leading to concurrent enhancements in both CL and $^1O_2$ generation. Subsequently, the folate-mediated cellular uptake performance of Cy7-EOM SS NMs was investigated in 4T1 cells through fluorescence analysis, by using confocal laser scanning microscopy (CLSM). As displayed in the CLSM images, the fluorescence intensity of 4T1 cells increased significantly over time, indicating effective cellular uptake, and reached a plateau at 6 hours according to fluorescence statistical data (Fig. S15). To confirm the promoting effect of folate on the cellular uptake of Cy7-EOM SS NMs, 4T1 cells were pre-treated with free folate molecules before incubation with Cy7-EOM SS NMs. Confocal images and corresponding statistical data showed that 4T1 cells pre-treated with folate exhibit a weaker red fluorescence signal than those without treatment, which is mainly because the premature binding of folate molecules to folate receptors on the cancer cell membrane hindered the binding of folate in the nanomaterials to folate receptors, thereby interfering with the cell uptake of Cy7-EOM SS NMs (Fig. S16). And due to the much higher expression level of folate receptors on a cancer cell membrane, nano-micelles are more likely to enter cancer cells than AML 12 cells, mouse normal liver cells (Fig. S17). After entering cancer cells, Cy7-EOM SS NMs would degrade under the high concentration of intracellular GSH and release Cy7-EOM. As GSH consumption can not only lead to the release of Cy7-EOM, but can also enhance the PDT effect in a synergetic manner, the level of intracellular GSH was analyzed using a fluorescence probe, 3-naphthalene-dicarboxaldehyde (NDA). CLSM images showed that the fluorescence intensity of NDA in 4T1 cells incubated with Cy7/CPPO NMs, Cy7-EOM NMs or Cy7-EOM SS NMs decreased to different degrees, and Cy7-EOM SS NMs performed best in terms of GSH consumption (Fig. S18). Then the targeting ability of released Cy7-EOM to mitochondria was evaluated through a mitochondrial co-localization experiment by using MitoTracker Green, a commercial mitochondrial labeling probe. As shown in confocal images, bright yellow signals were observed, resulting from the superposition of the red signal from Cy7-EOM and the green signal from Mito-Tracker Green. The line scanning profiles and the Pearson's correlation coefficient (ρ, calculated to be 0.90) from the co-localization scatter plot suggested the excellent targeting ability of the photosensitizer Cy7-EOM to mitochondria (Fig. 3c). Subsequently, Cy7-EOM will react with intracellular H_2O_2 to generate $^1O_2$ through ICET, which was verified by SOSG. CLSM images and corresponding fluorescence quantitative statistics showed that Cy7-EOM NMs have a higher $^1O_2$ yield than Cy7/CPPO NMs, providing further evidence for the higher efficiency of ICET than intermolecular energy transfer. Notably, 4T1 cells treated with Cy7-EOM SS NMs exhibit the brightest green fluorescence (Fig. 3d and S19). This is because, besides ICET, the release of Cy7-EOM mitigates the adverse effects of ACQ and the physical barrier against $^1O_2$ diffusion.

ROS burst and apoptosis mechanism

As mitochondria are one of the most important organelles in the cell and approximately 90% of intracellular ROS is generated in mitochondria, $^1O_2$ generation in mitochondria *in situ* will directly cause mitochondrial dysfunction and promote a series of cascade reactions, including a drop in mitochondrial membrane potential (MMP), the release of cytochrome C, and the activation of caspase 3—leading to ROS burst and eventually cell apoptosis. Thus, the mechanism of Cy7-EOM SS NMs induced apoptosis was studied in detail. Firstly, JC-1 staining was employed to investigate the change in MMP by CLSM. From the confocal images, we can see that obvious green fluorescence of JC-1 monomer emerged in 4T1 cells with treatment by Cy7-EOM NMs and Cy7-EOM SS NMs, and the highest ratio of green/red fluorescence intensity in the Cy7-EOM SS NMs group indicated the maximum MMP drop and most serious mitochondrial damage (Fig. 3e and S20). Subsequently, the release of cytochrome C and activation of caspase 3 induced by mitochondrial depolarization were evaluated and confirmed by immunofluorescence staining, which further demonstrated the most severe cell apoptosis induced by Cy7-EOM SS NMs (Fig. S21 and S22). Then, the total amount of ROS in 4T1 cells with different treatments was detected by DCFH-DA to verify ROS burst. As displayed in the confocal images, the strongest fluorescence intensity was observed in 4T1 cells treated with Cy7-EOM SS NMs, and the sharp rise in ROS concentration verified the domino burst (Fig. 3f and S23). GSH consumption and ROS burst will lead to an increase in intracellular levels of GSSG, and the GSH/GSSG ratio is commonly used as an indicator of cellular toxicity.[48,49] The results showed that the GSH/GSSG ratio in cancer cells treated with Cy7-EOM SS NMs was the lowest, which was mainly due to the synergetic effects of both GSH consumption by SS bonds in the nano micelles and the most efficient production of singlet oxygen, demonstrating the best therapeutic effect of Cy7-EOM SS NMs (Fig. S24). Then apoptosis was investigated with live/dead cells using calcein acetoxymethyl ester (Calcein AM)/propidium iodide (PI) double staining and flow cytometry analysis of Annexin V-FITC/PI

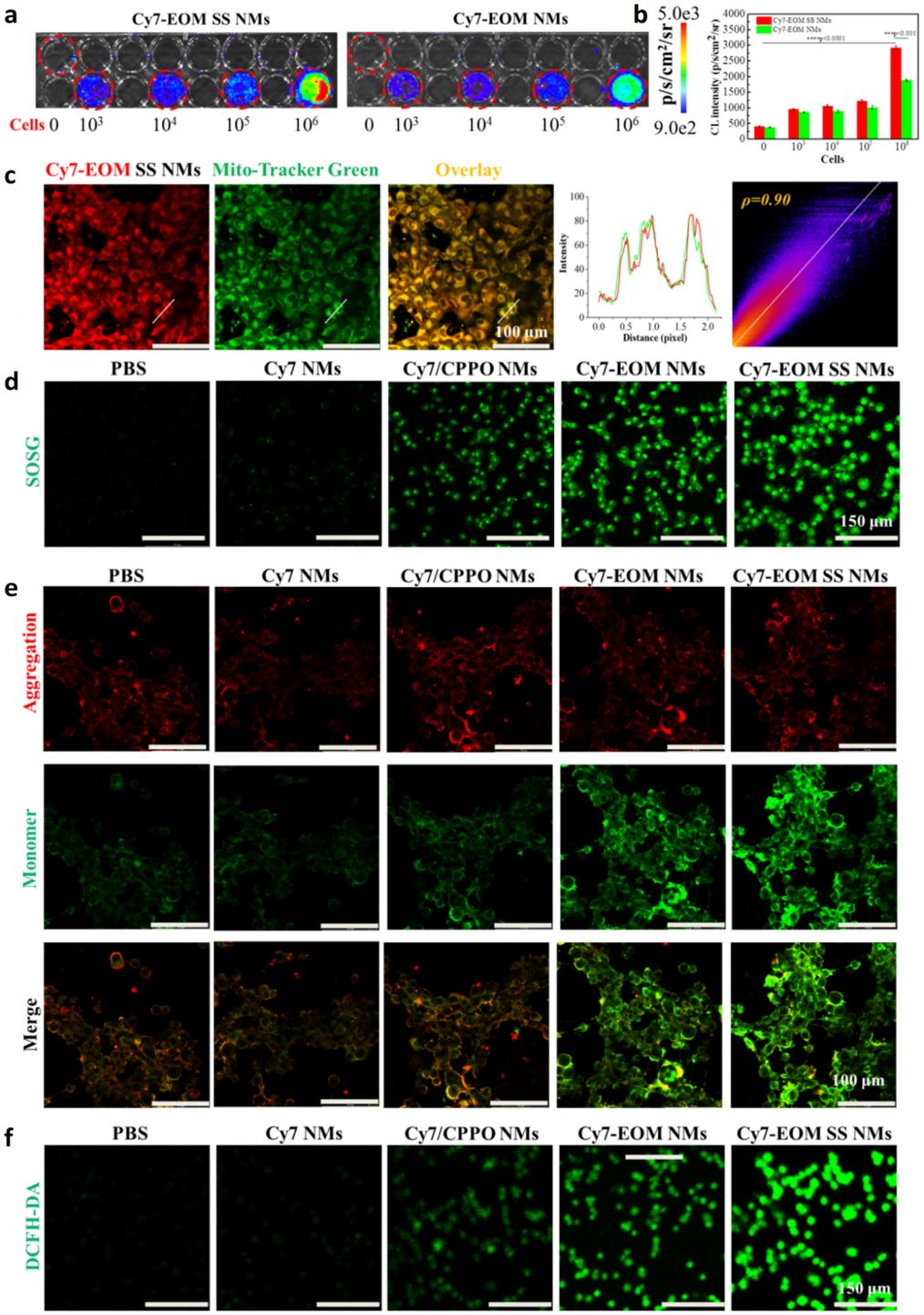

Fig. 3 Mitochondrial targeting and ROS generation of the Cy7-EOM SS NMs. (a) Chemiluminescence images of different amounts of 4T1 cells treated with Cy7-EOM SS NMs and Cy7-EOM NMs. (b) Corresponding quantitative data of CL intensity. (c) Co-localization experiments of Cy7-EOM SS NMs with MitoTracker Green labelled mitochondria. Scale bars are 100 μm. The quantification of fluorescent intensity of the line scanning profiles and fluorescence scatter diagram in the corresponding confocal images. (d) CLSM images of 4T1 cells stained by SOSG (1 μM) after different treatments. Scale bars are 150 μm. (e) CLSM images of 4T1 cells stained by JC-1 (10 μM, red for aggregate and green for monomer) after different treatments. Scale bars are 100 μm. (f) CLSM images of 4T1 cells stained by DCFH-DA (10 μM) after different treatments. Scale bars are 150 μm. Data are reported as the means ± S.D. and analyzed by two-tailed Student's *t*-test.

staining. CLSM images and the corresponding fluorescence statistical quantization showed that the largest percentage of cell deaths appeared in the cells treated by Cy7-EOM SS NMs (Fig. 4a and S25). Similarly, in the flow cytometry data, the proportion of $FITC^+/PI^+$ 4T1 cells is 81.91%, higher than the 66.76% of 4T1 treated with Cy7-EOM NMs or 23.08% of 4T1 cells

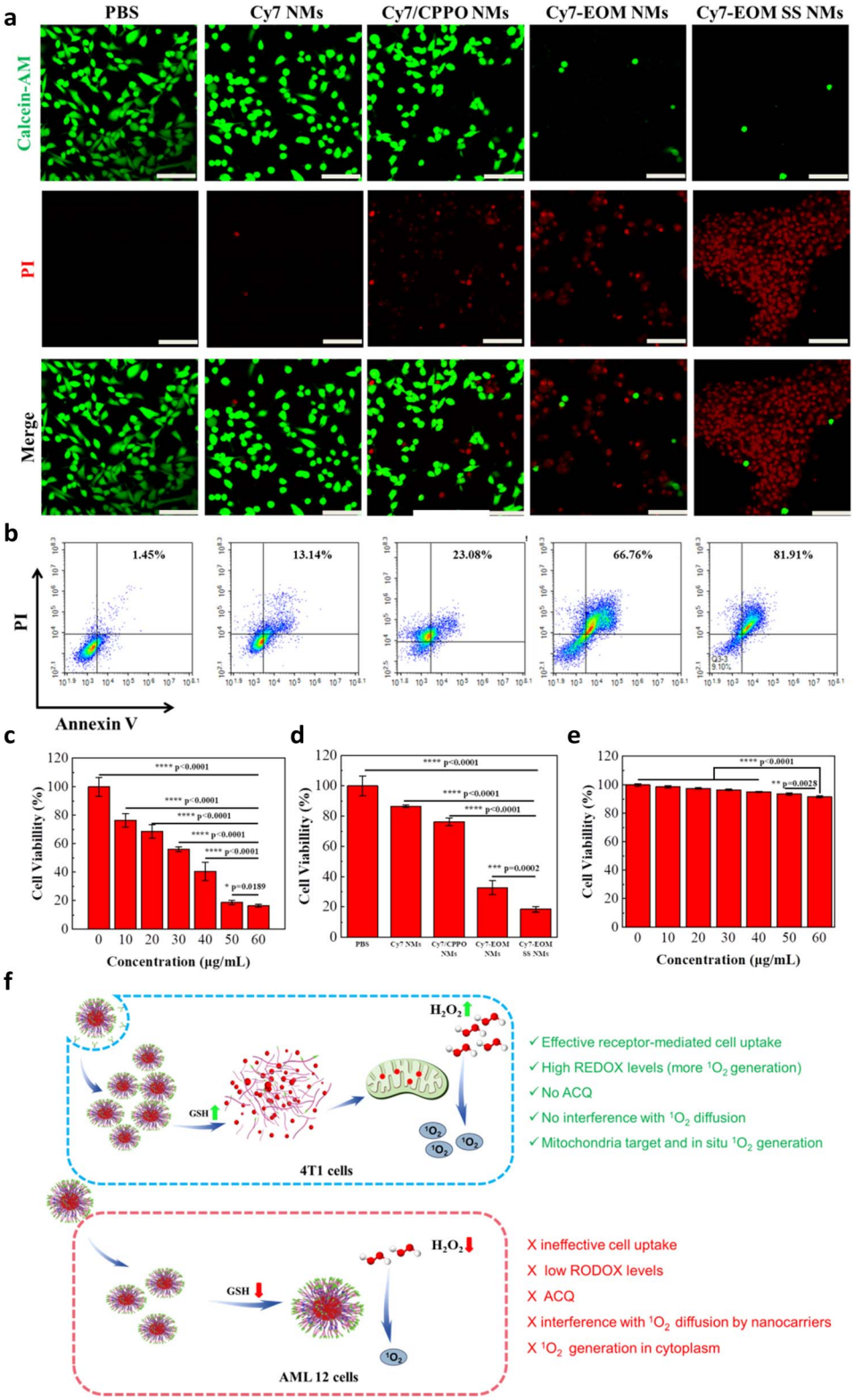

Fig. 4 Intracellular anticancer efficiency of the Cy7-EOM SS NMs. (a) Live/dead cell co-staining assays of 4T1 cells after different treatments, using Calcein-AM (10 μM) and PI (10 μM) as indicators, Scale bars are 200 μm. (b) Cell apoptosis assessment with Annexin V-FITC/PI by flow cytometry analysis after different treatments. (c) The viabilities of 4T1 cells treated with Cy7-EOM SS NMs with different concentrations. (d) The viabilities of 4T1 cells with different treatments with a concentration of 50 μg mL^{-1} (e) The viabilities of AML 12 cells treated with Cy7-EOM SS NMs of different concentrations. (f) Schematic illustration of the difference in the toxicity of Cy7-EOM SS NMs to 4T1 cells and AML 12 cells. Data are reported as the means ± S.D. and analyzed by two-tailed Student's *t*-test.

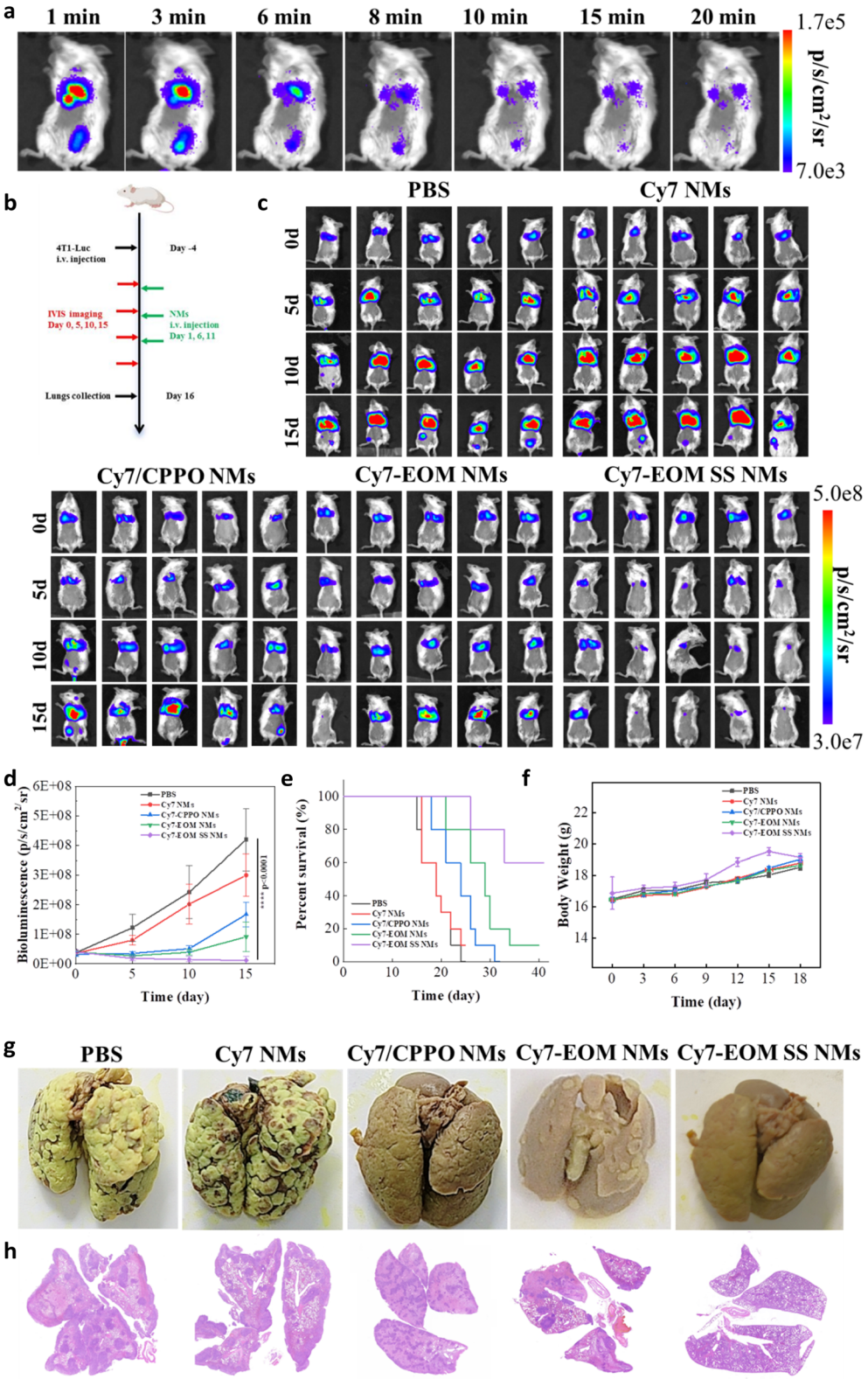

Fig. 5 *In vivo* anti-tumor effects against metastatic tumors. (a) Chemiluminescent images of mice with intravenous injection of Cy7-EOM SS NMs. (b) The schedule of the therapeutic process. (c) Bioluminescence images of mice receiving different treatments, $n = 5$. (d) Curves of tumor cell bioluminescence intensity in the lungs of mice after different treatments, $n = 5$. (e) Survival curves of mice after different treatments $n = 10$. (f) Body weights of mice in each group during treatment, $n = 10$. (g) Representative lung photographs stained by Bouin fixative solution after different treatments. (h) Representative H&E staining images of the lungs of mice in different groups. Data are reported as the means ± S.D. and analyzed by two-tailed Student's *t*-test.

treated with Cy7/CPPO NMs, suggesting its superior PDT efficiency compared to the others (Fig. 4b). The cytotoxicity of Cy7-EOM SS NMs was also evaluated by a methyl thiazolyl tetrazolium (MTT) assay. As shown in Fig. 4c, the viability of 4T1 cells decreased significantly with an increasing concentration of Cy7-EOM SS NMs, and the viability was as low as 18.44% at a concentration of 50 μg mL^{-1}, while the viabilities of 4T1 treated with Cy7 NMs, Cy7/CPPO NMs and Cy7-EOM NMs were much higher (86.5%, 76.1% and 32.6%, respectively) (Fig. 4d). The half maximal inhibitory concentration (IC50) of the photosensitizer drug on cancer cells was calculated to be 33.54 μg mL^{-1} (Fig. S26). By comparison, negligible cell death was observed in AML 12 cells treated by Cy7-EOM SS NMs, even at high incubation concentrations (Fig. 4e). According to the above results, this significant difference is determined by multiple factors, and the detailed mechanism is illustrated in Fig. 4f.

In vivo CL imaging and treatments of metastatic tumors

Encouraged by the excellent therapeutic effect on cancer cells and extremely low side effects on normal cells, the anti-tumor efficiency of Cy7-EOM SS NMs was then assessed *in vivo*. Before that, the stability of Cy7-EOM SS NMs under the condition of physiological levels of GSH in the bloodstream was first studied by employing DLS analysis to detect the size change after the nano-micelles were incubated with GSH (10 μM) for 12 h. DLS results showed no obvious change in the hydrodynamic diameter after Cy7-EOM SS NMs were incubated with GSH, indicating their good stability during blood circulation (Fig. S27). The half-time in blood circulation of Cy7-EOM SS NMs was calculated to be 2.06 h through fluorescence analysis (Fig. S28). Then, the ability of nanomaterials to perform targeted imaging and diagnosis was verified. Mouse models of lung metastases were established by intravenous injection of Luciferase-transfected 4T1 cells (4T1-Luc). As shown in the fluorescence images, after intravenous injection of Cy7-EOM SS NMs, a clear chemiluminescence signal was observed in the lung. It is worth noting that there is also a chemiluminescence signal in the abdominal cavity (Fig. 5a and S29). In order to determine the reason, the mouse was euthanized and autopsied and we found that new metastatic tumor sites could be observed in the intestines (Fig. S30). The results showed that the designed Cy7-EOM SS NMs possess distinct targeting capability and high responsiveness to a low concentration of H_2O_2. This exceptional performance enables high-sensitivity imaging and accurate diagnosis, even for detecting small secondary metastatic tumors. Then the anti-tumor effects were evaluated; the detailed treatment schedule is shown in Fig. 5b. The mice were randomly divided into five groups with different treatments with PBS, Cy7 NMs, Cy7/CPPO NMs, Cy7-EOM NMs and Cy7-EON SS NMs at a dosage of 2.5 mg kg^{-1} each. Bioluminescence imaging was employed for evaluation of the therapeutic effects. As shown, the bioluminescence intensity of the mice treated with PBS and Cy7 NMs increased significantly, and there was a new metastasis site in the abdominal cavity, indicating rapid tumor progression. By comparison, Cy7/CPPO NMs, Cy7-EOM NMs and Cy7-EOM SS NMs treated mice showed obvious inhibition of tumor growth. Among them, Cy7-EOM SS NMs performed best and the bioluminescence intensity decreased to 9.8% compared with that in the PBS group (Fig. 5c and d). In particular, mice in the groups treated with PBS, Cy7 NMs and Cy7/CPPO NMs showed multiple metastatic tumor sites in the intestines, while a faint bioluminescence signal in the lung and no bioluminescence signal in the abdominal cavity were observed in mice treated with Cy7-EOM SS NMs, demonstrating its great potential as a drug for the treatment of metastatic tumors and even multiple metastatic tumors. After 15 days of treatment, the lungs in each group were dissected. Photographs and hematoxylin-eosin (H&E) staining also demonstrated that the lungs in the PBS, Cy7 NMs, and Cy7-EOM NMs groups were occupied by more metastatic tumor nodules, while almost no metastatic foci could be observed in the Cy7-EOM SS NMs group (Fig. 5g and h). In addition, after treatment with Cy7-EOM SS NMs, the lifespan of the mice was greatly extended, and 60% of the mice survived for more than 40 days, while almost all the mice in the control group died within 25 days (Fig. 5e). We then conducted a comprehensive analysis of the potential toxicity of the photosensitizer drug, which is critical for further application. As shown in photographs and weight analysis, there was no noticeable skin phototoxicity in the dorsal skin of mice under normal conditions with 12 hours of light and dark cycles for 7 days in the Cy-EOM SS NMs group, characterized by erythema and edema (Fig. S31 and S32). H&E staining of five major organs (heart, liver, spleen, lung, and kidney) was conducted for histological toxicity analyses and no tissue damage was observed (Fig. S33). Moreover, the results of biochemical and routine blood tests showed no statistically significant variation in key markers indicative of live function (ALT and AST), liver function (BUN and CRE), and routine blood parameters (Fig. S34 and S35). The mouse weights in each group were monitored during the treatment and there was no obvious decrease in body weight, further confirming the safety of Cy7-EOM SS NMs (Fig. 5f). The extremely low side effects were mainly due to the low concentration of H_2O_2 in normal tissues, which cannot effectively produce $^1O_2$. Additionally, in normal tissues with a low level of GSH, the nano-micelles maintained their integrity, which caused ACQ of the photosensitizer and had a shielding effect on the diffusion of $^1O_2$.

Conclusions

In this study, to address the current issue of the shallow penetration depth of the excitation light in PDT and the challenge of its application in the treatment of metastatic tumors in clinical settings, a chemiluminescence method was adopted as the excitation light to develop an efficient self-supplying photosensitizer molecule Cy7-EOM by covalently coupling the energy donor peroxyoxalate derivative with the receptor photosensitizer. The covalent coupling of the donor and the receptor in the molecular structure significantly enhances the efficiency of PDT. Under high concentrations of H_2O_2 in the tumor microenvironment, PDT can be autonomously activated *in situ*, overcoming the limitations of traditional PDT, which suffers from shallow penetration depth and is ineffective against deep

tissue metastatic tumors. Cy7-EOM was encapsulated into a tumor-specific response nano-micelle Cy7-EOM SS-NMs-FA for targeted delivery and release. In cancer cells, Cy7-EOM SS-NMs-FA would consume large amounts of reducing GSH, leading to degradation and the release of Cy7-EOM, which specifically targets mitochondria. The generated ROS then act directly on the mitochondria, inducing mitochondrial ROS bursts that trigger cell apoptosis. This approach has been successfully applied to treat breast cancer cells and multiple metastatic tumors in mice, achieving efficient PDT of metastatic tumors and extremely low systemic toxicity. These findings expand the practical application range of photosensitizers and offer new strategies for photodynamic anticancer drugs, with significant potential for clinical translation.

Ethical statement

All animal experiments were performed in compliance with the relevant guidelines and regulations of the People's Republic of China for the care and use of experimental animals (Regulations on the Administration of Laboratory Animals of the People's Republic of China). All animal experiments were approved by Ethics Committee of Medical College of Qingdao University (QDU-AEC-2025550).

Author contributions

H. Z. and H. L. contributed equally to this work. Z. Y. conceived the study. Z. Y., H. Z. and H. L. designed the experiments. H. Z., H. L. and H. W. conducted the chemical syntheses. H. Z. and H. L. prepared the nanomaterials and conducted the *in vitro* characterization. H. Z., H. L., M. X., Y. W. and J. Z. conducted the cell experiments. Z. Y., H. L. and Y. T. performed the *in vivo* experiments. Z. Y., H. Z., H. L., Y. T., H. W. and B. T. analyzed the data. Z. Y., Y. T., and B. T. drafted the manuscript.

Conflicts of interest

There are no conflicts to declare.

Data availability

All data included in this study are available upon request from the corresponding author. Supplementary information (SI): materials, instruments and figures. See DOI: https://doi.org/10.1039/d5sc09043a.

Acknowledgements

This work was supported by National Natural Science Foundation of China (21904075, 22377113), the Natural Science Foundation of Shandong Province (ZR2020YQ15) and Taishan Scholar Program of Shandong Province (tsqn202306103).

References

1 J. Massagué and A. C. Obenauf, Metastatic colonization by circulating tumour cells, *Nature*, 2016, **529**, 298–306.
2 S. Kiri and T. Ryba, Cancer, metastasis, and the epigenome, *Mol. Cancer*, 2024, **23**, 154.
3 P. Priestley, J. Baber, M. P. Lolkema, N. Steeghs, E. d Bruijn, C. Shale, K. Duyvesteyn, S. Haidari, A. v Hoeck, W. Onstenk, P. Roepman, M. Voda, H. J. Bloemendal, T. Heijnen, M. Labots, P. O. Witteveen, E. F. Smit, S. Sleijfer, E. E. Voest and E. Cuppen, Pan-cancer whole-genome analyses of metastatic solid tumours, *Nature*, 2019, **575**, 210–216.
4 A. W. Lambert, Y. Zhang and R. A. Weinberg, Cell-intrinsic and microenvironmental determinants of metastatic colonization, *Nat. Cell Biol.*, 2024, **26**, 687–697.
5 K. Ganesh and J. Massagué, Targeting metastatic cancer, *Nat. Med.*, 2021, **27**, 34–44.
6 E. Karimi, M. W. Yu, S. M. Maritan, L. J. M. Perus, M. Rezanejad, M. Sorin, M. Dankner, P. Fallah, S. Doré, D.-m. Zuo, B. Fiset, D. J. Kloosterman, L. Ramsay, Y.–h. Wei, S. Lam, R. Alsajjan, I. R. Watson, G. R. Urgoiti, M. Park, D. Brandsma, D. L. Senger, J. A. Chan, L. Akkari, K. Petrecca, M. C. Guiot, P. M. Siegel, D. F. Quail and L. A. Walsh, A Single-cell spatial immune landscapes of primary and metastatic brain tumours, *Nature*, 2023, **614**, 555–563.
7 D. Asanuma, M. Sakabe, M. Kamiya, K. Yamamoto, J. Hiratake, M. Ogawa, N. Kosaka, P. L. Choyke, T. Nagano, H. Kobayashi and Y. Urano, Sensitive β-galactosidase-targeting fluorescence probe for visualizing small peritoneal metastatic tumours in vivo, *Nat. Commun.*, 2015, **6**, 6463.
8 J. Kim, S. Lee, Y. Kim, M. Choi, I. Lee, E. Kim, C. Gyu Yoon, K.-Y. Pu, H. Kang and J. S. Kim, In situ self-assembly for cancer therapy and imaging, *Nat. Rev. Mater.*, 2023, **8**, 710–725.
9 M.-le Li, Y.-J. Xu, X.-J. Peng and J. S. Kim, From Low to No O_2-Dependent Hypoxia Photodynamic Therapy (hPDT): A New Perspective, *Acc. Chem. Res.*, 2022, **55**, 3253–3264.
10 Y.-F. Tang, Y.-Y. Li, B. Li, W.-T. Song, G.-B. Qi, J.-W. Tian, W. Huang, Q.-L. Fan and B. Liu, Oxygen-independent organic photosensitizer with ultralow-power NIR photoexcitation for tumor-specific photodynamic therapy, *Nat. Commun.*, 2024, **15**, 2530.
11 X.-Z. Zhao, J.-P. Liu, J.-L. Fan, H. Chao and X.-J. Peng, Recent progress in photosensitizers for overcoming the challenges of photodynamic therapy: from molecular design to application, *Chem. Soc. Rev.*, 2021, **50**, 4185–4219.
12 T. C. Pham, V. Nguyen, Y. Choi, S. Lee and J. Yoon, Recent Strategies to Develop Innovative Photosensitizers for Enhanced Photodynamic Therapy, *Chem. Rev.*, 2021, **121**, 13454–13619.
13 Y.-Y. Yin, X.-Y. Ge, J. Ouyang and N. Na, Tumor-activated in situ synthesis of single-atom catalysts for O_2-independent

photodynamic therapy based on water-splitting, *Nat. Commun.*, 2024, **15**, 2954.
14 M. So, C.-J. Xu, A. M. Loening, S. S. Gambhir and J.-H. Rao, Self-illuminating quantum dot conjugates for in vivo imaging, *Nat. Biotechnol.*, 2006, **24**, 339–343.
15 D. W. Felsher, Cancer revoked: oncogenes as therapeutic targets, *Nat. Rev. Cancer*, 2003, **3**, 375–380.
16 X.-S. Li, J. F. Lovell, J. Yoon and X.-Y. Chen, Clinical development and potential of photothermal and photodynamic therapies for cancer, *Nat. Rev. Clin. Oncol.*, 2020, **17**, 657–674.
17 J.-S. Huang, L.-C. Su, C. Xu, X.-G. Ge, R.-P. Zhang, J.-B. Song and K.-Y. Pu, Molecular radio afterglow probes for cancer radiodynamic theranostics, *Nat. Mater.*, 2023, **22**, 1421–1429.
18 X.-Z. Wang and K.-y Pu, Molecular, substrates for the construction of afterglow imaging probes in disease diagnosis and treatment, *Chem. Soc. Rev.*, 2023, **52**, 4549–4566.
19 Y.-Y. Jiang and K.-Y. Pu, Molecular Probes for Autofluorescence-Free Optical Imaging, *Chem. Rev.*, 2021, **121**, 13086–13131.
20 M.-W. Yang, Z.-L. Zeng, J. W. Y. Lam, J.-L. Fan, K.-Y. Pu and B.-Z. Tang, State-of-the-art self-luminescence: a win-win situation, *Chem. Soc. Rev.*, 2022, **51**, 8815–8831.
21 C.-Z. Ran and K.-Y. Pu, Molecularly generated light and its biomedical applications, *Angew. Chem., Int. Ed.*, 2024, **63**, e202314468.
22 Z.-Z. Yu, P. Zhou, W. Pan, N. Li and B. Tang, A biomimetic nanoreactor for synergistic chemiexcited photodynamic therapy and starvation therapy against tumor metastasis, *Nat. Commun.*, 2018, **9**, 5044.
23 J.-S. Huang, C. Zhang, X. -Z Wang, X. Wei and K.-Y. Pu, Near-Infrared Photodynamic Chemiluminescent Probes for Cancer Therapy and Metastasis Detection, *Angew. Chem., Int. Ed.*, 2019, **58**, 10660–10665.
24 G. Obaid, J. P. Celli, M. Broekgaarden, A. Bulin, P. Uusimaa, B. Pogue, T. Hasan and H.-C. Huang, Engineering photodynamics for treatment, priming and imaging, *Nat. Rev. Bioeng.*, 2024, **2**, 752–769.
25 G.-H. Lu, X.-J. Wang, F. Li, S. Wang, J.-E. Zhao, J.-Y. Wang, J. Liu, C.-L. Lyu, P. Ye, H. Tan, W.-P. Li, G.-H. Ma and W. Wei, Engineered biomimetic nanoparticles achieve targeted delivery and efficient metabolism-based synergistic therapy against glioblastoma, *Nat. Commun.*, 2022, **23**, 4214.
26 M.-W. Yang, J.-G. Huang, J.-L. Fan, J.-J. Du, K.-Y. Pu and X.-J. Peng, Chemiluminescence for bioimaging and therapeutics: recent advances and challenges, *Chem. Soc. Rev.*, 2020, **49**, 6800–6815.
27 J.-H. Lou, X.-F. Tang, H.-K. Zhang, W.-J. Guan and C. Lu, Chemiluminescence Resonance Energy Transfer Efficiency and Donor-Acceptor Distance: from Qualitative to Quantitative, *Angew. Chem., Int. Ed.*, 2021, **60**, 13029–13034.
28 Y.-J. Wang, L.-N. Shi, Z.-F. Ye, K. Guan, L.-L. Teng, J.-H. Wu, X. Yin, G.-S. Song and X.-B. Zhang, Reactive Oxygen Correlated Chemiluminescent Imaging of a Semiconducting Polymer Nanoplatform for Monitoring Chemodynamic Therapy, *Nano Lett.*, 2020, **20**, 176–183.
29 J.-J. Ding, G.-H. Lu, W.-D. Nie, L.-L. Huang, Y.-H. Zhang, W.-L. Fan, G.-H. Wu, H.-L. Liu and H.-Y. Xie, Self-Activatable Photo-Extracellular Vesicle for Synergistic Trimodal Anticancer Therapy, *Adv. Mater.*, 2021, **33**, 2005562.
30 A. J. Shuhendler, K.-Y. Pu, L.-N. Cui, J. P. Uetrecht and J.-H. Rao, Real-time imaging of oxidative and nitrosative stress in the liver of live animals for drug-toxicity testing, *Nat. Biotechnol.*, 2014, **31**, 373–380.
31 X. Jie, H.-M. Yang, M. Wang, Y. Zhang, W.-L. Wei and Z.-N. Xia, A Peroxisome-Inspired Chemiluminescent Silica Nanodevice for the Intracellular Detection of Biomarkers and Its Application to Insulin-Sensitizer Screening, *Angew. Chem., Int. Ed.*, 2017, **56**, 14596–14601.
32 Y.-L. Yang, S.-F. Wang, L.-F. Lu, Q.-S. Zhang, P. Yu, Y. Fan and F. Zhang, NIR-II Chemiluminescence Molecular Sensor for In Vivo High-Contrast Inflammation Imaging, *Angew. Chem., Int. Ed.*, 2020, **59**, 18380–18385.
33 Z.-X. Chen, L.-C. Su, Y. Wu, J.-Y. Liu, R.-R. Wu, Q. Li, C.-L. Wang, L.-T. Liu and J.-B. Song, Design and Synthesis of a Small Molecular NIR-II Chemiluminescence Probe for in Vivo-Activated H_2S Imaging, *Proc. Natl. Acad. Sci. U. S. A*, 2023, **120**, e2205186120.
34 L. Li, X.-Y. Zhang, Y.-X. Ren, Q. Yuan, Y.-Z. Wang, B.-K. Bao, M.-Q. Li and Y.-L. Tang, Chemiluminescent Conjugated Polymer Nanoparticles for Deep-Tissue Inflammation Imaging and Photodynamic Therapy of Cancer, *J. Am. Chem. Soc.*, 2024, **146**, 5927–5939.
35 P. Li, L. Liu, H.-B. Xiao, W. Zhang, L.-L. Wang and B. Tang, A New Polymer Nanoprobe Based on Chemiluminescence Resonance Energy Transfer for Ultrasensitive Imaging of Intrinsic Superoxide Anion in Mice, *J. Am. Chem. Soc.*, 2016, **146**, 2893–2896.
36 L. Yang, M. Zhao, W. Chen, J.-L. Zhu, W.-N. Xu, Q. Li, K.-Y. Pu and Q.-Q. Miao, A Highly Bright Near-Infrared Afterglow Luminophore for Activatable Ultrasensitive In Vivo Imaging, *Angew. Chem., Int. Ed.*, 2024, **63**, e202313117.
37 H.-J. Ning, Y.-X. Yang, C.-Y. Lv, D.-D. Zhou, S.-R. Long, W. Sun, J.-J. Du, J.-L. Fan and X.-J. Peng, Hydrogen peroxide-activatable iodoBodipy-phthalhydrazid conjugate nanoparticles for cancer therapy, *Nano Res.*, 2023, **16**, 12294–12303.
38 X.-Q. Xu, H.-J. An, D.-L. Zhang, H. Tao, Y. Dou, X.-H. Li, J. Huang and J.-X. Zhang, A self-illuminating nanoparticle for inflammation imaging and cancer therapy, *Sci. Adv.*, 2019, **5**, eaat2953.
39 H.-J. An, C.-H. Guo, D.-D. Li, R.-F. Liu, X.-Q. Xu, J.-W. Guo, J. Ding, J.-J. Li, W. Chen and J.-X. Zhang, Hydrogen Peroxide Activatable Nanoparticles for Luminescence Imaging and In Situ Triggerable Photodynamic Therapy of Cancer, *ACS Appl. Mater. Interfaces*, 2020, **12**, 17230–17243.
40 D. Mao, W.-B. Wu, S.-L. Ji, C. Chen, F. Hu, D.-L. Kong, D. Ding and B. Liu, Chemiluminescence-Guided Cancer Therapy Using a Chemiexcited Photosensitizer, *Chem*, 2017, **3**, 991–1007.

41 H.-S. Shen, F.-Y. Sun, X.-Y. Zhu, J.-Y. Zhang, X.-W. Ou, J.-Q. Zhang, C.-H. Xu, I. D. Williams, S.-J. Chen, R. T. K. Kwok, J. W. Y. Lam, J.-W. Sun, F. Zhang and B.-Z. Tang, Rational Design of NIR-II AIEgens with Ultrahigh Quantum Yields for Photo- and Chemiluminescence Imaging, *J. Am. Chem. Soc.*, 2022, **144**, 15391–15402.

42 D. Ding, C. C. Goh, G.-X. Feng, Z.-Z. Zhao, J. Liu, R.-R. Liu, N. Tomczak, J.-L. Geng, B.-Z. Tang, L.-G. Ng and B. Liu, Ultrabright Organic Dots with Aggregation-Induced Emission Characteristics for Real-Time Two-Photon Intravital Vasculature Imaging, *Adv. Mater.*, 2013, **25**, 6083–6088.

43 S. S. Lucky, K. C. Soo and Y. Zhang, Nanoparticles in Photodynamic Therapy, *Chem. Rev.*, 2015, **115**, 1990–2042.

44 M. Klaper, W. Fudickar and T. Linker, Role of Distance in Singlet Oxygen Applications: A Model System, *J. Am. Chem. Soc.*, 2016, **138**, 7024–7029.

45 Q.-Q. Min, Z.-H. Ni, M. You, M. Liu, Z. Zhou, H.-T. Ke and X.-Y. Ji, Chemiexcitation-Triggered Prodrug Activation for Targeted Carbon Monoxide Delivery, *Angew. Chem., Int. Ed.*, 2022, **61**, e202200974.

46 M. Usama, C.-M. Lin and K. Burgess, On the Mechanisms of Uptake of Tumor-Seeking Cyanine Dyes, *Bioconjugate Chem.*, 2018, **29**, 3886–3895.

47 R. Tian, X. Feng, L. Wei, D.-J. Dai, Y. Ma, H.-F. Pan, S.-X. Ge, L. Bai, C.-M. Ke, Y.-L. Liu, L.-X. Lang, S.-J. Zhu, H. Sun, Y.-B. Yu and X.-Y. Chen, A genetic engineering strategy for editing near-infrared-II fluorophores, *Nat. Commun.*, 2022, **13**, 2853.

48 D. M. Townsend, K. D. Tew and H. Tapiero, The importance of glutathione in human disease, *Biomed. Pharmacother.*, 2003, **57**, 145–155.

49 S. Carelli, A. Ceriotti, A. Cabibbo, G. Fassina, M. Ruvo and R. Sitia, Cysteine and Glutathione Secretion in Response to Protein Disulfide Bond Formation in the ER, *Science*, 1997, **299**, 1681–1684.